Formula graph self-attention network for representation-domain independent materials discovery

*Achintha Ihalage and Yang Hao**

Achintha Ihalage
School of Electronic Engineering and Computer Science
Queen Mary University of London
Mile End Rd
Bethnal Green, London E1 4NS
Email Address: a.a.ihalage@qmul.ac.uk

Prof. Yang Hao
School of Electronic Engineering and Computer Science
Queen Mary University of London
Mile End Rd
Bethnal Green, London E1 4NS
Email Address: y.hao@qmul.ac.uk
(*Corresponding author)

Keywords: *graph-network, attention, epsilon-near-zero, materials-informatics, machine-learning*

Abstract

The success of machine learning (ML) in materials property prediction depends heavily on how the materials are represented for learning. Two dominant families of material descriptors exist, one that encodes crystal structure in the representation and the other that only uses stoichiometric information with the hope of discovering new materials. Graph neural networks (GNNs) in particular have excelled in predicting material properties within chemical accuracy. However, current GNNs are limited to only one of the above two avenues owing to the little overlap between respective material representations. Here, we introduce a new concept of formula graph which unifies both stoichiometry-only and structure-based material descriptors. We further develop a self-attention integrated GNN that assimilates a formula graph and show that the proposed architecture produces material embeddings transferable between the two domains. Our model substantially outperforms previous structure-based GNNs as well as structure-agnostic counterparts while exhibiting better sample efficiency and faster convergence. Finally, the model is applied in a challenging exemplar to predict the complex dielectric function of materials and nominate new substances that potentially exhibit epsilon-near-zero phenomena.

Graphical Abstract for Table of Contents

A new concept of formula graph is proposed as a general representation of crystal structure and chemical composition for graph neural networks (GNNs). This enables implementing a novel self-attention integrated GNN that is applicable in both structure-based and structure-agnostic materials property prediction schemes, solving a long-standing problem of maintaining separate machine learning architectures for each domain.

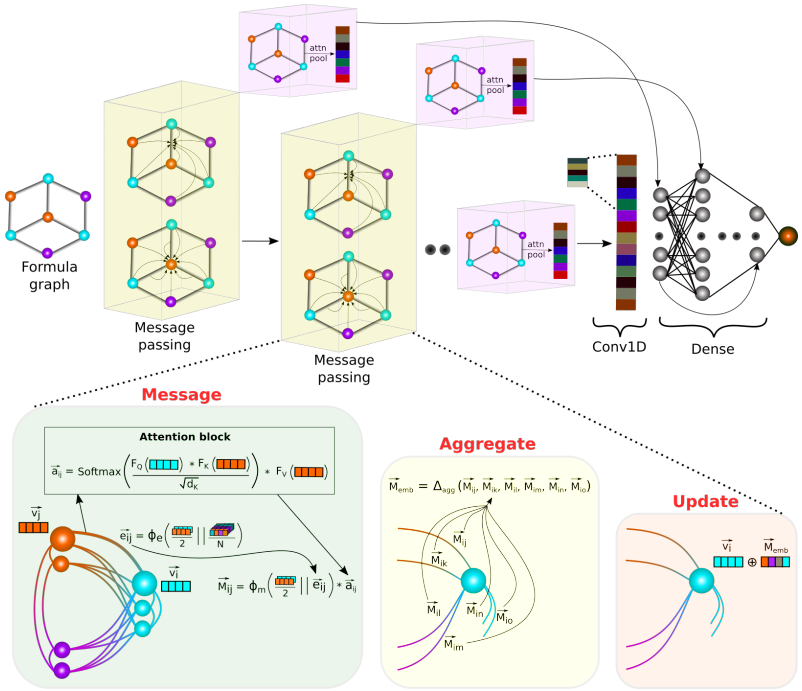

1 Introduction

The quest for functional materials has spiked during the last few years marking a paradigm shift in materials design which has traditionally been a laborious process. One major landmark is the emergence of computational methods such as density functional theory (DFT) that can accurately estimate material properties from the smallest repeating unit of constituent atoms. This has shown great promise in discovering materials with target properties by eliminating redundant experimental cycles. However, DFT operates on characterised crystal structures which are usually unknown for the materials yet to be discovered. Moreover, the computational effort of DFT scales as the cube of system size ($O(n^3)$),[1,2] presenting a serious handicap in material exploration. Diversifying the applications of known materials and discovering new ones with desired properties is the highway to advance technologies. This calls for a fast and unified approach which breaks the traditional boundary of material science and enables us to predict material properties only from the stoichiometry, but also infer uncharacterised properties when the crystal structure is available.

Machine learning (ML) has made rapid inroads into materials science as surrogate models that can learn a complex mapping from a fixed-shape material descriptor to a target property. The dominance of ML in materials informatics propelled by curated databases is evident not only because of successful instances in new materials discovery, but also due to its significant impact on every step of material design hierarchy.[3–6] This includes replacing first-principles calculations,[7–13] optimal design of experiments,[14–16] material characterisation[17–19] and improved understanding of material phenomena.[20–22] While hand-crafted material descriptors warrant uniqueness and invariance to translations, rotations and permutations of constituents, the performance of ML models is heavily reliant on how fine the descriptor is and the level of chemical and structural information captured.[23] Structure-agnostic descriptors are the key to access an unexplored material terrain, however, this assumes that all materials are in their most stable form (i.e. crystal structure with the lowest energy per atom). Therefore, metastable polymorphs are not attainable. Structure-based descriptors on the other hand can encode polymorphs and generally yield much better ML performance, but they are restricted only to characterised crystals. Many compounds have arbitrary number of atoms and element types. This means conventional material representations are inevitably limited by varying-size to fixed-size conversion efficiency.

Ordered nature of crystalline materials exhibits a natural graph where atoms represent nodes and the interactions between them indicate edges. Graph neural network (GNN) is an ideal candidate to obtain a global representation of a material by exchanging information between neighbouring nodes and edges while preserving the original graph through several layers. This alleviates the drawback of prior descriptors by automatically learning a material encoding based on data. To this end, seminal works have proposed various graph convolutional architectures to learn chemical and geometric features of molecules and/or crystals. Notably, MPNN,[24] SchNet,[25] CGCNN[11] and MegNet[12] models have shown excellent performance in predicting diverse material properties. All models were found to execute almost equally well, especially when ample training data is available.[26] Structure-based representation domain is further enriched by a plethora of other GNN architectures[27–30] and physically intuitive descriptors.[31,32]

While crystal structure can be directly mapped into a graph, devising a graph from the stoichiometry alone requires intuitive reasoning. `Roost` is a structure-agnostic GNN model that represents stoichiometric formula as a dense weighted graph between elements.[33] It has achieved impressive error rates when predicting the formation energy of inorganic compounds. Unfortunately, the two types of GNN models that exist in materials literature are not interchangeable. That is because structure-based GNNs are not designed to take chemical composition as the only input whereas structure-agnostic models intentionally disregard the crystal structure. Currently, this problem has demanded extra computer resources and workload in maintaining separate ML models for respective domains. This technology gap has also hindered domain transferability and direct evaluation of the effect of crystal structure in prediction

performance on top of what is achievable by stoichiometry based models because ML architectures adopted in both processes are simply different.

Here, we introduce formula graph, a versatile representation of crystalline materials based on chemical formula that can also take crystal structure into consideration when available. In the structure-agnostic domain, our key intuition is to obtain integer formula of the material and treat every atom as an individual node in a fully connected graph. The edge weights are estimated during training. Such a process ensures that the stoichiometry is preserved and the edge predictions work towards improving the overall performance. On the other hand, a crystal graph can be generalised as a formula graph containing the unit cell formula. Because geometry information is available in this case, edge attribute is characterised by the actual distance between the two atoms that form the edge. This simple distinction between formula-only and structure-based representations permits us to design a more general GNN that can bridge the gap between the two avenues of materials property prediction.

We hereby develop a universal ML model, `Finder` (**F**ormula graph self-attent**i**on **n**etwork for materials **d**iscov**er**y), to predict material properties using formula alone or by accounting the crystal structure, independently. `Finder` is a message passing GNN that adopts a variant of self-attention mechanism in the transformer architecture.[34] We show that `Finder` outperforms state-of-the-art stoichiometry-only models such as `Roost` as well as crystal graph models such as `MegNet` and `CGCNN` on diverse benchmark databases curated from the Materials Project (MP) repository. Compared to other models revisited in this work, our model displays faster convergence and achieves lower error rates at all training set sizes explored.

One area which the GNNs have not yet been particularly challenged is the prediction of material properties in the form of a complex function. As a challenging and timely application, we investigate `Finder`'s competence in predicting the frequency-dependent dielectric function of materials from the JARVIS DFT repository.[35] Subsequently, we identify promising epsilon-near-zero (ENZ) materials with operating frequencies ranging from near infra-red (NIR) to ultra-violate (UV) regions. Our results highlight the compounds containing vanadium oxoanions as an exciting class of materials for low loss ENZ candidacy. ENZ materials display exotic properties such as nonlinear electro-optical phenomena[36–38] that facilitate harmonic generation,[39] wave mixing,[40] ultrafast optical switching[41] and phase-tunable metasurface design.[42] Despite the limited size of training database, our model can accurately predict the dielectric function of materials without the use of crystal structure, making it a powerful materials discovery platform at any given scale.

2 Results

An important virtue of our representation is to account every atom in the chemical formula as a separate node as opposed to canonical descriptors that couple element types with their molar fraction. A crystal unit cell contains one or more integer formula units (Z). This is the motivation behind our formula graph representation as it provides means to unify various graph based material descriptors. Formula graph allows neighbouring node information to flow through edges towards the parent node via a series of message passing operations. Message passing is a powerful feature extracting method that consolidates some simple mathematical operations applied on the graph with function approximators learned from data. Therefore, node embeddings learned after a stack of message passing layers will be globally aware of the constituent atomic species as well as the data context. In what follows, we use the term “formula graph" to denote integer formula graph or unit cell formula graph (i.e. crystal graph) in general whereas specific terms will be used when needed to differentiate between these two concepts.

We first initialise each node of formula graph with an atom-specific numeric vector, identified as node attribute. Node attributes can be manually derived based on element properties or, they can be extracted as learned element embeddings from a ML model trained on vast amount of materials data. While the former representation is more interpretable, latter ensures that the vectors are properly normalised, compressed, and some chemical and contextual information about the elements is captured. In the structure-agnostic case, our formula graph is fully connected. Structure-based formula graph is obtained by connecting the atoms that are located at a distance less than a threshold radius. Depending on crystal structure, this may or may not yield a fully connected graph.

Figure 1 displays the conversion of an example material $Cu_2Ag_2O_3$ to its formula graphs. $Cu_2Ag_2O_3$ crystallizes in tetragonal $I4_1/amd$ structure as shown in Figure 1a. Its primitive unit cell contains two formula units ($Z = 2$) indicating that crystal graph can be much larger than its integer formula counterpart and therefore selective bonding of atoms is necessary to minimise computational complexity. Figure 1b shows the binary adjacency matrix extracted by applying the threshold radius over the distance matrix of the crystal. The region highlighted in cyan colour indicates the atoms that are connected in the crystal graph. The integer formula graph of the example material, as depicted in Figure 1c contains seven atoms whereas the crystal graph (Figure 1d) consists of fourteen atoms connected with strong bonds, reflecting the unit cell of the material.

`Finder`’s core architecture is designed with several attention-integrated message passing layers followed by a global pooling layer to learn context-specific material descriptor from the formula graph. The computation inside our message passing layer involves three steps - message, aggregate and update. The node attributes are updated according to the formula

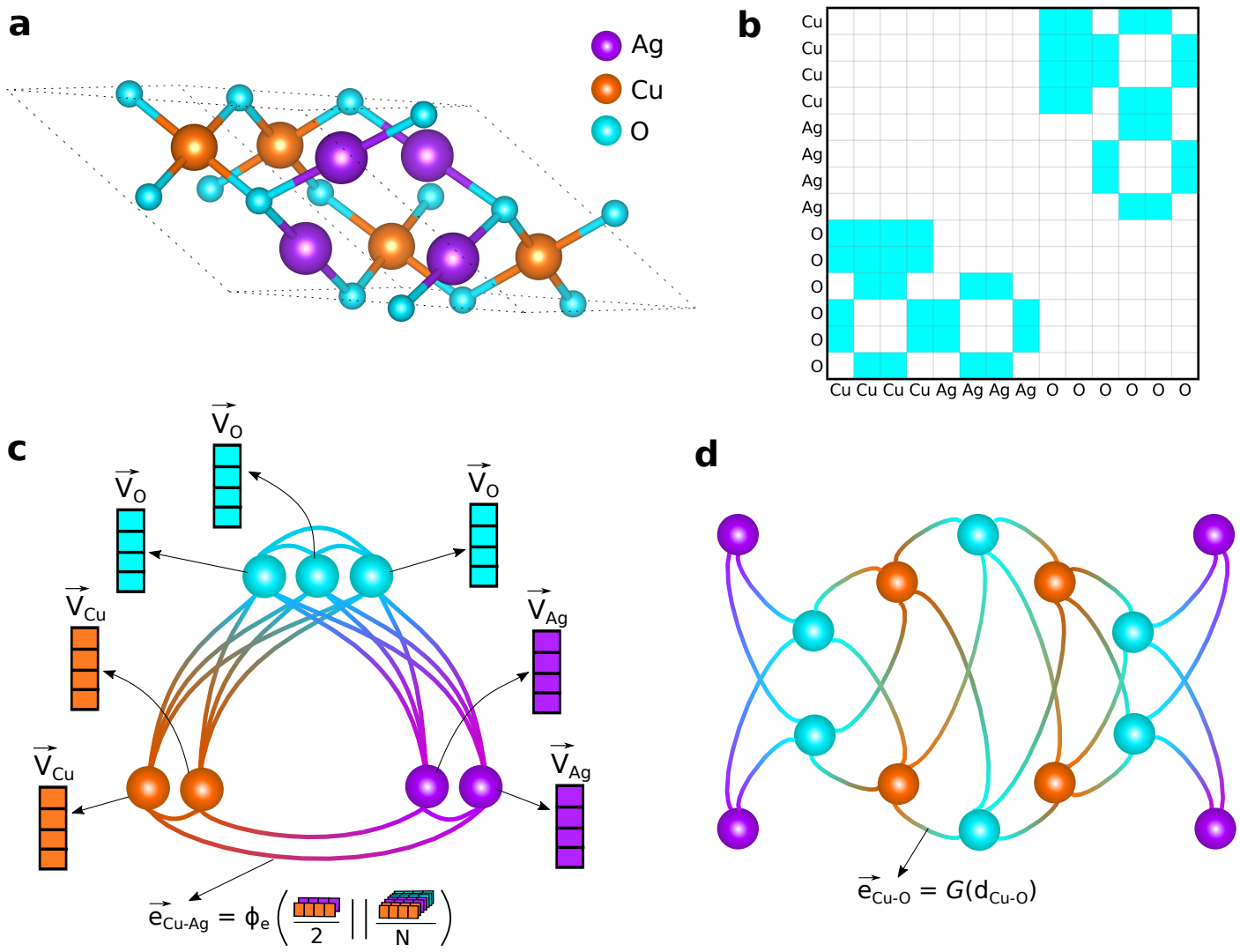

Figure 1: Formula graph representation. (a) Crystal structure of $Cu_2Ag_2O_3$ in $I4_1/amd$ space group symmetry. (b) Adjacency matrix of the crystal. Shaded cells indicate pairs of atoms with atomic spacing less than 2.5 Å. (c) Integer formula graph of the example material. Each node carries an element-specific node attribute. The edge attributes are predicted by a neural network whose input is an aggregation of the associated node attributes. Note that although a single connection between any two nodes is shown for simplicity, the integer formula graph is directional and the edges are bi-directional. This means, for example, e_{Cu-Ag} is not necessarily equal to e_{Ag-Cu}. (d) Simplified crystal graph constructed from the adjacency matrix in (b). Here, we use the Gaussian expansion of actual distance between atoms as the edge attribute. This is an undirectional graph.

$$v_i{}^{r+1} = f_u\left(v_i{}^r, f_a\left(\sum_{j\in C_i} f_m\left(v_i{}^r, v_j{}^r\right)\right)\right) \tag{1}$$

where $v_i{}^r$ is the node attribute vector of node i after r number of updates, C_i is the set of neighbours of node i and f_m, f_a and f_u are the message, aggregate and update functions, respectively. During the message step, a message vector M_{ij}^r between two connected nodes i and j is generated. The first move towards obtaining M_{ij}^r is to determine the edge attribute vector e_{ij}^r between nodes i and j. In the

structure-agnostic domain, we estimate e_{ij}^r on the fly during training time as follows;

$$e_{ij}^r = \phi_e \left[\left(\frac{v_i^r \oplus v_j^r}{2} \right) \Big|\Big| \left(\frac{1}{N_i} \sum_{k \in C_i} \frac{v_i^r \oplus v_k^r}{2} \right) \right] \tag{2}$$

where ϕ_e is a feed-forward neural network with two hidden layers, N_i is the total number of neighbours of node i and, $\oplus$ and $||$ denote element-wise summation and concatenation operators, respectively. This edge predictive function ensures that the edge attribute draws information not only from the two atoms that form the edge, but also from all other atoms available in the formula graph. If the crystal structure is considered, e_{ij}^r is simply calculated as the Gaussian expansion G of the atomic distance d_{ij} between nodes i and j.

$$e_{ij}^r = G\left(d_{ij}\right) \tag{3}$$

`Finder` employs a variant of self-attention mechanism to compute an alignment score vector a_{ij}^r between every pair of nodes (i, j). Self-attention has excelled especially in natural language processing (NLP) by allotting a certain attention to different words in a sequence in order to obtain a more robust representation of the same sequence. Because the ordering of atoms is irrelevant in our formula graph, we calculate element-wise alignment scores that account the importance of other constituent atoms when creating the message M_{ij}^r. This involves following steps;

$$QK_{ij}^r = \exp\left(\frac{F_Q\left(v_i^r\right) \odot F_K\left(v_j^r\right)}{\sqrt{d_K}} \right) \tag{4}$$

$$a_{ij}^r = \left(\frac{QK_{ij}^r}{\sum_{l=1}^{N} QK_{il}^r} \right) \odot F_V\left(v_j^r\right) \tag{5}$$

where F_Q, F_K and F_V denote single-hidden-layer neural networks applied on the neighbouring node attributes to obtain query, key and value vectors, respectively. d_K is the dimension of key vector and $\odot$ symbols element-wise product. Likewise, the proposed attention mechanism deviates from the scalar dot product attention in the transformer model.[34] In this work, we use a single attention head. Each entry in a_{ij}^r is normalised considering all nodes (N) in the formula graph. Finally, M_{ij}^r is obtained by processing all attribute vectors involved in forming a message via another two-hidden-layer neural network ϕ_m and regularising its output by the alignment scores as follows.

$$M_{ij}^r = \phi_m \left(\left(\frac{v_i^r \oplus v_j^r}{2} \right) \Big|\Big| e_{ij}^r \right) \odot a_{ij}^r \tag{6}$$

We notice that using the element-wise mean as a function to merge two node attributes (e.g. $\frac{v_i^r \oplus v_j^r}{2}$) yields better performance than the concatenation function (e.g. $v_i^r || v_j^r$) because the mean is naturally permutation-invariant, normalised, and it retains the original dimension of the vectors.

In the aggregate step, messages around each node are aggregated using another permutation-invariant function Δ_{agg}. We use the element-wise mean as the aggregate function in this work. Finally, the node attribute is updated by adding the aggregated vector to the current node attribute transformed through a trainable weight matrix W_{int} to equate the dimensions. Figure 2 summarises the operations within a message passing layer and the overall architecture.

$$v_i^{r+1} = v_i^r . W_{int} + \Delta_{agg} \left(M_{i0}^r, M_{i1}^r, ..., M_{iN\_i}^r \right) \tag{7}$$

After P number of message passing layers, we apply an attention-based pooling layer $attn\_pool$ that is invariant to the indexing of atoms to obtain a fixed-length global representation V_M of the material. Our $attn\_pool$ layer is inspired from that of `Roost`, however, element weighting is not required in our model because formula graph already carries this information. We probe every message passing layer through separate $attn\_pool$ layers in order to make residual connections to latter layers of the network. Therefore, our model has P number of global pooling layers that help propagate features extracted at different levels of abstraction.

$$V_M = attn\_pool \left(v_0^r, v_1^r, ..., v_N^r \right) \tag{8}$$

The learned representation V_M is then sent through a standard convolutional layer and a set of fully connected layers with residual connections to produce the final output. The model is trained to minimise L_1 robust loss[33] between the predictions and the targets. We note that robust loss is less sensitive to the outliers and it yields better performance compared to the standard mean absolute error (MAE) or mean squared error (MSE) loss functions. It also enables quantifying the aleatoric uncertainty of predictions (i.e. inherent uncertainty due to the probabilistic variability). This approach evaluates model uncertainty in a single run whereas quantifying the epistemic uncertainty caused by a lack of knowledge about the best model requires several runs and can be too computationally expensive.[33] Nevertheless, we use the MAE as the performance metric to benchmark our model against those from the literature.

2.1 Benchmark datasets

We curate six datasets from the Materials Project (MP) database relating to DFT computed properties - formation energy per atom (E_f), final energy per atom (E_{DFT}), bandgap (E_g), refractive index (n), bulk modulus (K_{VRH}) and shear modulus (G_{VRH}). Because composition to property mapping should be uniquely defined, we only record the property value for the lowest energy (E_{DTF}) polymorph. Therefore,

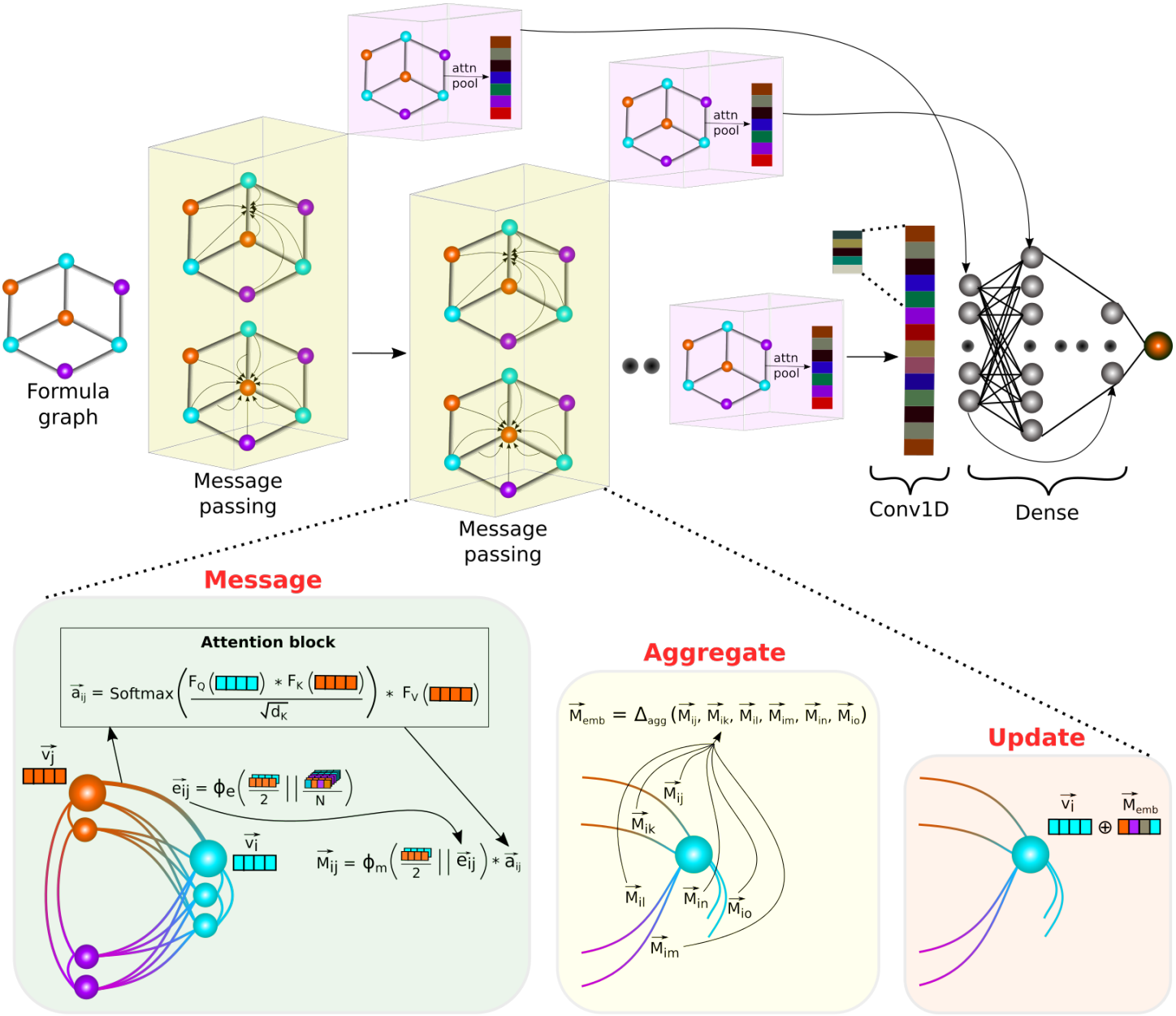

Figure 2: The architecture of Finder and message passing layer operations. `Finder` expects a formula graph as input which is processed through several message passing layers followed by a post-processing neural network. Each message passing layer is coupled with a global attention pooling layer to enable residual connections to latter layers. Message phase executes the core operations of our architecture. Specifically, by predicting all directional edge attributes e_{ij}^r, we allow information to cascade from neighbouring nodes to the edges. These edge features along with end-node attributes v_i^r and v_j^r contribute to a message vector, M_{ij}^r. Each entry of M_{ij}^r is already weighted by a self-attention mechanism that quantifies the importance of other nodes for the current message vector. Aggregate step summarises all messages around a given node via a local pooling function. Finally at the update step, the aggregated message vector is added to the initial node attribute completing one cycle of information flow.

none of the datasets contain other polymorphs or duplicate compositions. Using the same databases for both structure-based `Finder` and structure-agnostic counterpart facilitates direct comparison of these two models as well. All datasets are split into 70% training, 15% validation and 15% test sets. The models are trained on the training set, the best model is selected by evaluating on the validation set and finally the performance (MAE) on the test set is reported. The distributions of train, validation and test data of all benchmark databases are shown in Supporting Figure S1.

2.2 Structure-agnostic model evaluation

As machine learning toolbox is constantly enriched with more powerful architectures such as GNNs, the worth of classical ML in materials informatics, or even convolutional neural networks (CNNs) for that matter is sometimes overlooked. Here, we employ a random forest model trained with *Magpie* composition representations as the baseline model (`RF_Magpie`).[10] *Magpie* features carry a wealth of known information about the elements in a composition. We further implement a deep residual neural network optimised with several standard 1-D convolutional layers followed by a series of fully connected layers as the deep learning baseline (`ResCNN`). This model only takes a vector of element fractions as its input. In this section, we evaluate structure-agnostic `Finder` model on six benchmark datasets and compare it with `Roost`, `ResCNN` and `RF_Magpie` models.

Table 1 summarises the MAEs of `Finder` and other structure-agnostic models on the same test set. It can be observed that `Finder` outperforms all other models irrespective of material property or dataset size. `Roost` produces impressive results too. We identify several focal points of our model that elevates its performance above that of `Roost`. First, our formula graph inherently encodes the stoichiometry whereas the representation of `Roost` requires propagating the fractional element weights to the message passing layer and the model performance might depend on where and how the fractional weights are injected. Second, similar to actual distance between two atoms in a crystal structure depends on other atoms in the crystal, our edge predictive function fetches information from all other atoms in the formula graph to estimate edge attributes. This may in turn result in a more robust global representation of the material. Third, transformer-based self-attention component in our model includes trainable function approximators that enable abstracting the node attributes in different subspaces. This allows gaining a more vivid representation of the constituent atomic species before assigning an attention score to each of them.

Notably, `ResCNN` displays good MAE values despite operating on extremely simple material descriptors that only contain element fractions. This is possibly because standard convolutional layers are still remarkable feature extractors, and descriptor to property mapping function is potentially simplified by the use of a simple descriptor. Nevertheless, the performance of `ResCNN` and `RF_Magpie` that use fixed-length descriptors is always lower than that of graph-based models demonstrating the power of GNNs in

	Finder	Roost	ResCNN	RF_Magpie
E_f (68699)	**0.0858 ± 0.0004**	0.0913	0.1125	0.1434
E_{DFT} (68699)	**0.0896 ± 0.0001**	0.097	0.1278	0.2059
E_g (68699)	**0.2911 ± 0.0009**	0.3243	0.3535	0.3319
n (3920)	**0.1726 ± 0.004**	0.1902	0.1989	0.3277
$log(K_{VRH})$ (7025)	**0.0835 ± 0.0006**	0.0852	0.0913	0.0936
$log(G_{VRH})$ (7025)	**0.1153 ± 0.0014**	0.1231	0.127	0.1234

Table 1: MAEs of structure-agnostic models in predicting six benchmark properties. The results for Finder are based on three separate runs. Same training, validation and test sets are used in evaluating all models. E_f and E_{DFT} are in eV/atom, E_g is in eV and K_{VRH} and G_{VRH} are in GPa. The training progress comparison of Finder and Roost is shown in Supporting Figure S2.

representing diverse material compositions.

Materials data, especially experimental measurements are often limited by size. This raises concerns on the competence of GNNs or ML models in general to learn from largely undersampled datasets and yet provide fairly accurate out-of-database predictions. In order to evaluate the sample efficiency of Finder, we observe its performance under different training set sizes. Figure 3 depicts formation energy prediction MAE curves of all structure-agnostic models. Finder achieves the lowest error scores at all training set levels ranging from 10^2 to $\sim$ 7x10^4. Classical ML models that use explainable features such as RF_Magpie are generally known to work well with small data. Despite inheriting from deep learning regime, our model starts outperforming RF_Magpie as the training set size hits 10^2. While the MAE curve of Finder always hovers below that of Roost, the two error curves have a similar gradient. The distance between these two curves can be interpreted as the performance gain and our model offers 13 meV reduction in error on average compared to Roost. The threshold energy criterion (i.e. energy above convex hull, E_{hull}) that decides the thermodynamic stability of materials is about 25 meV[43] which is also similar to the error of DFT formation energies relative to the experiments.[44] Therefore, we believe the accuracy improvement in our model could be vital in discovering new stable materials.

The E_f parity plot shown in Figure 4a indicates that structure-agnostic Finder makes acceptable individual predictions, especially when the target value is negative. This is due to the large number of negative E_f samples available in the MP database. Computational materials databases tend to report more stable materials that usually have a negative E_f than the materials having a positive E_f which are typically unstable. As expected, the aleatoric uncertainty of relatively inaccurate predictions is higher than that of the samples lying close to perfect prediction line.

One key advancement of our network architecture is the simultaneous prediction of edge attributes from the associated node embeddings during training. We investigate whether these predicted edge values indeed capture some chemical or structural insights which are not explicitly fed to the model. Figure 4c

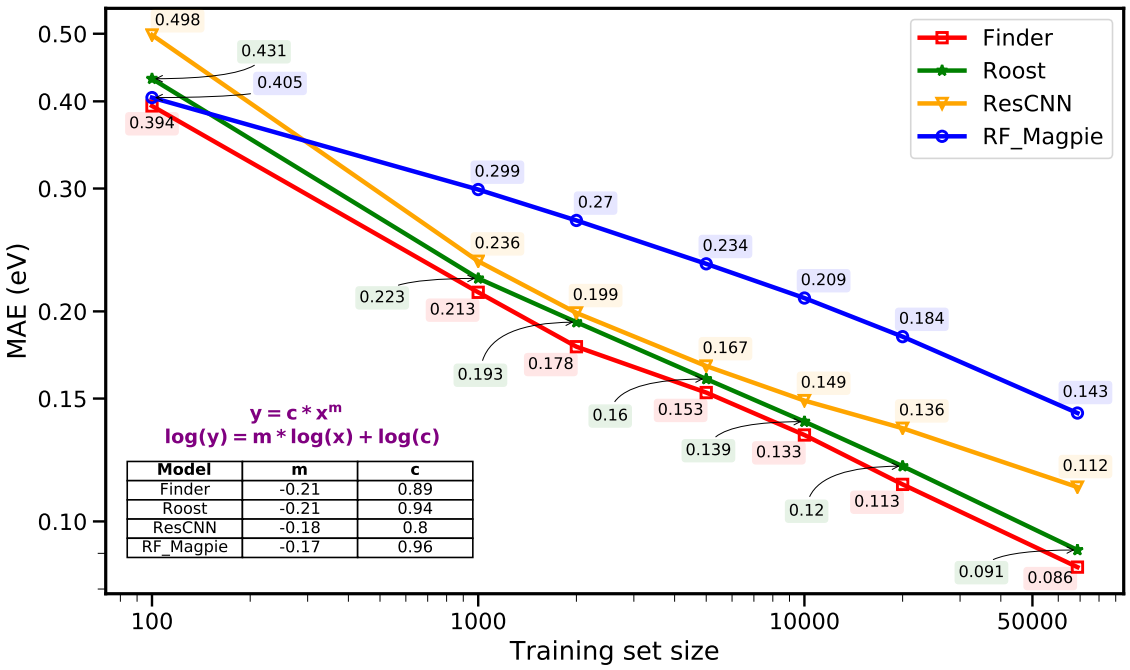

Figure 3: Sample efficiency evaluation of structure-agnostic models on the MP formation energy dataset. Both axes are in log scale. The predictions in general abide by the power law.[45] By fitting to a power law function as shown in the figure, we obtain similar gradients for the error curves of `Finder` and `Roost` ($m = -0.21$). The absolute gradient is understandably smaller for `ResCNN` and `RF_Magpie`.

presents edge attribute matrices (EAMs) of four well known perovskites, obtained from the final message passing layer of the trained E_f and n models, respectively. One might think of EAM as formula-domain relative of crystal-domain distance matrix. However, at it stands, such comparison is implausible because crystal structure may have several formula units. Nevertheless, from the E_f model, we find that compositionally and structurally similar materials such as $SrTiO_3$ and $BaTiO_3$ have similar EAMs. Intriguingly, compositionally different, yet structurally similar perovskite $KNbO_3$ is found to have a comparable EAM to the ones above. The EAM of halide perovskite $CsPbI_3$ is considerably different from its oxide counterparts. Consistent trend is observed from the refractive index model, yet resulting in different EAMs for the same material. Obviously, EAM entries are determined by the constituent element types and the data context. Although individual edge attributes carry no physical meaning, certain analogies between compositions can still be recovered from the EAM. Recently, we have shown that quantifying materials analogies can accelerate target driven discovery of materials.[13] Such analogies rely on stoichiometry-derived global material embeddings. Incorporating EAMs that reflect interactions between atoms adds another dimension for materials similarity analysis.

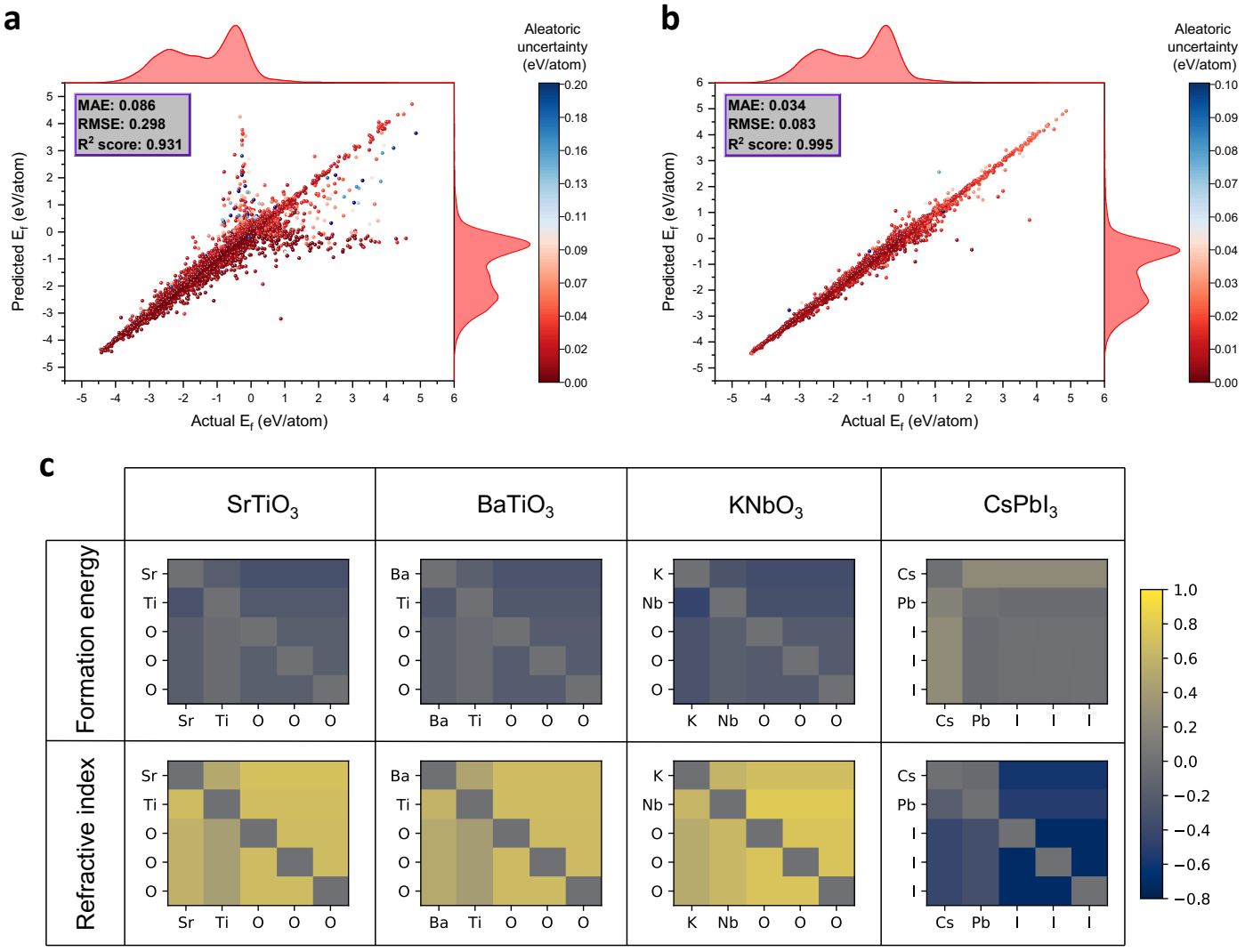

Figure 4: Parity plots of structure-agnostic `Finder` (a) and structure-based variant (b) as obtained for the formation energy test set. The inclusion of spatial distances to the formula graph has significantly reduced both the error and the uncertainty in predictions. The marginal distributions of test data and the predictions are shown on the secondary axes. RMSE - root mean squared error, R^2 score - coefficient of determination. Parity plots for the other properties are included in Supporting Figure S3 and Figure S4. (c) Edge attribute matrices of perovskite materials $SrTiO_3$, $BaTiO_3$, $KNbO_3$ and $CsPbI_3$ visualised by probing E_f and n `Finder` models. The EAM is not necessarily symmetric because e^r_{ij} is not always equal to e^r_{ji} (see Equation 2).

2.3 Structure-based model evaluation

In our formula graph representation, shifting from structure-agnostic domain to structure-based domain is as simple as replacing the edge attributes with Gaussian-expanded atomic spacings and de-densifying the graph by connecting only the atoms arranged locally within a certain distance. This permits us to use the same message passing architecture, and any improvement in performance over structure-agnostic results is merely due to the addition of crystal structure, more specifically, the atomic spacings. In this section, we examine the structure-based variant of `Finder` with other materials graph networks such as `MegNet` and `CGCNN`. Table 2 lists the MAEs of all structure-based models on the same benchmark datasets. `Finder` outperforms `CGCNN` in all properties and `MegNet` in four out of six properties. The decrease in error of our model is more prominent for relatively small datasets. This can be partly attributed to the self-attention component in our model that potentially makes the representation learning process more efficient by weighting the contribution from each individual atom in the crystal graph. Recent work also reveals that integrating attention into a neural network amplifies molecular property prediction performance in a data-limited regime.[46]

	Finder	MegNet	CGCNN
E_f (68699)	**0.0342** $\pm$ **0.0003**	0.0376	0.0423
E_{DFT} (68699)	0.0351 $\pm$ 0.0001	**0.0344**	0.088
E_g (68699)	0.2627 $\pm$ 0.001	**0.2598**	0.2921
n (3920)	**0.1513** $\pm$ **0.003**	0.163	0.2564
$log(K_{VRH})$ (7025)	**0.0728** $\pm$ **0.0003**	0.0736	0.0806
$log(G_{VRH})$ (7025)	**0.1028** $\pm$ **0.0013**	0.1098	0.1138

Table 2: MAEs of structure-based models in predicting six benchmark properties.

Overall, `Finder` and `MegNet` comfortably surpass quantum chemical accuracy (errors below 1 kcal/mol or equivalently 43 meV/atom[2]) in predicting formation energy and total energy of crystals. The MAEs of these models fall within the error of DFT against the experiments for all other properties E_g, n, K_{VRH} and G_{VRH}.[47–49] Figure 4b demonstrates the generalisability of our model for the E_f test set. This parity plot is less scattered compared to that of structure-agnostic `Finder` (Figure 4a) because geometric features convey ample information about material properties on top of what can be recovered from the chemical formula. Notably, incorporating crystal structure lowers E_f and E_{DFT} prediction errors by over 60%, a significant improvement from structure-agnostic results (see Table 1 and Table 2). Even a subtle variation in crystal structure may have a substantial effect on material properties. Therefore, a large and diverse database of crystals is desirable to effectively capture structure-property dependence. E_f and E_{DFT} datasets are sufficiently sized and well assorted with 224 space group symmetries to facilitate a more granular learning of structural features.

Surprisingly, structure-based bandgap prediction only observes about 10% reduction in error compared to formula-only counterpart. This underpins the fact that bandgap is a difficult quantity to predict even with modern DFT energy functionals,[50,51] demanding a certain degree of empiricism to counterpoise DFT errors.[52] We believe, the MAE of structure-agnostic `Finder` entering an acceptable error range of 0.25 - 0.3 eV for bandgap prediction,[47] and even slightly outperforming structure-based `CGCNN` is a significant milestone in discovering materials with target bandgap from the hypothetical compounds landscape. Noticing that overall, the error of structure-agnostic version of our model is similar to the error of `CGCNN` for all properties excluding formation energy is particularly encouraging.

The learning efficiency of a ML model is determined by how fast it reaches the convergence. An efficient learning model should ideally produce a lower error value relative to other competing models at any given point in the training cycle (epochs). Our model exhibits superior learning efficiency compared to `CGCNN` and `MegNet` as corroborated by formation energy training curves in Figure 5a. `Finder` reaches chemical accuracy as quickly as in 83 training epochs whereas `MegNet` takes about 285 epochs to touch that level. `CGCNN` usually settles just around chemical accuracy after about 800 epochs. Figure 5b shows the cumulative distribution functions (CDFs) of three structure-based models. 79.1% of predictions made by `Finder` is within the chemical accuracy, higher than `MegNet` (77.4%) and `CGCNN` (69.8%). The CDF of our model stays above that of other models before all curves start to overlap near an error value of 0.12 eV/atom implying that all models find it equally difficult to predict the E_f of the remaining portion of materials.

Figure 5c and Figure 5d refer to the t-distributed stochastic neighbour embedding (t-SNE)[53] visualisations of the internal representations of materials in the E_f test set, assembled from structure-agnostic and structure-based `Finder` models, respectively. Interestingly, both latent maps resemble each other quite closely. Because t-SNE is a more visualisation oriented algorithm that involves non-linear projection, we further perform principal component analysis (PCA) on the same data and observe a similar trend (PCA plots are provided in Supporting Figure S5). We investigate whether the location of the same material on both latent spaces is approximately similar by coupling the corresponding PCA components from the two domains. Figure 5e displays the correlation between the first principal components of the material embeddings obtained with and without crystal structure. Figure 5f shows the same data for the second principal components. We find that structure-agnostic and structure-based PCA components are highly correlated with a Pearson's correlation coefficient (r) of 0.96 between the first components and 0.94 between the second components. This means the two `Finder` models in general produce linearly related material embeddings where one is inferable from the other, although a few exceptions exist.

In structure-based domain, the latent vectors are expected to encode crystal structure details, and the

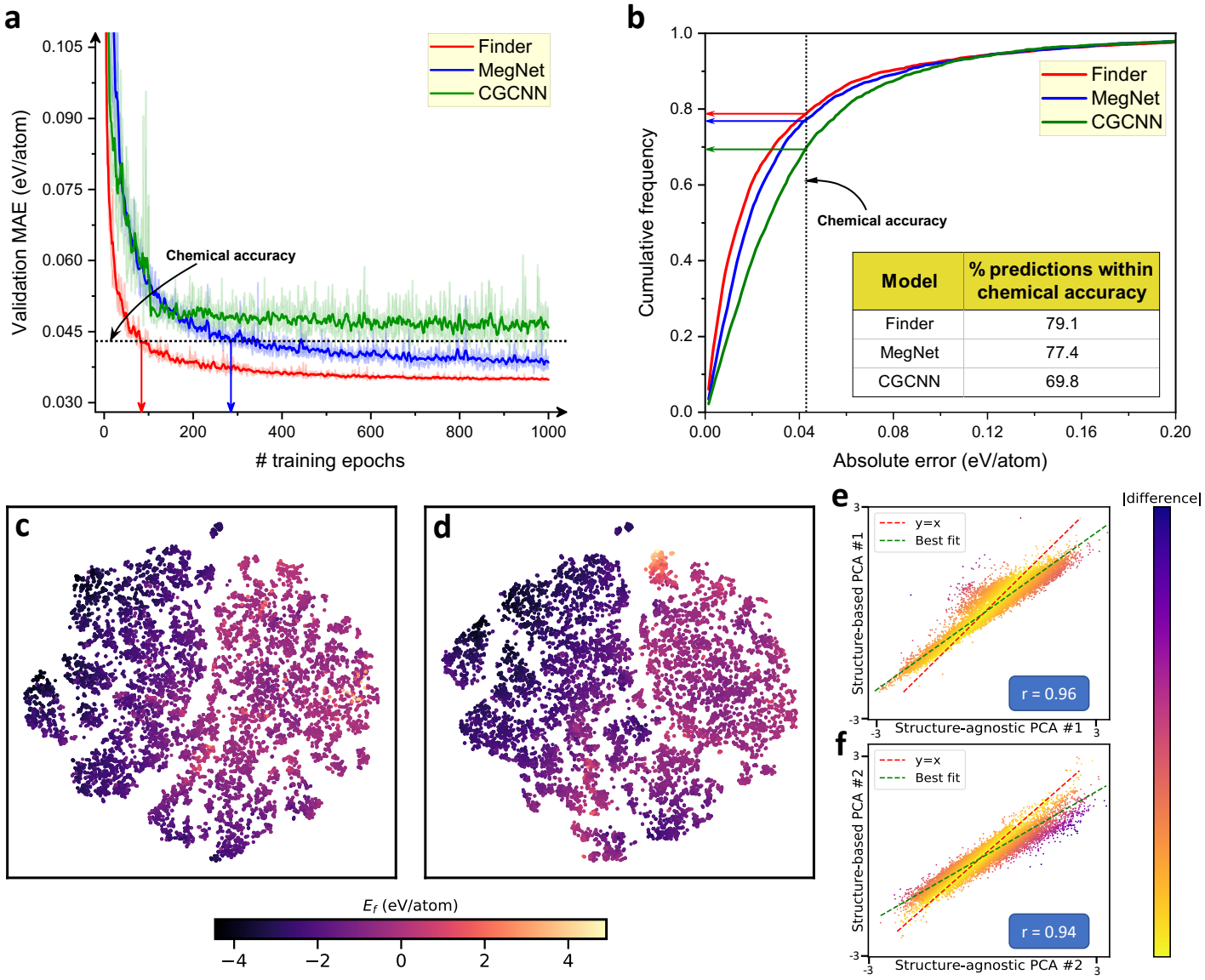

Figure 5: Learning efficiency evaluation and t-SNE/PCA visualisations of material embeddings for the E_f test set. (a) The training progress curves of `Finder`, `MegNet` and `CGCNN`. Shaded region represents the standard deviation of MAEs. (b) Cumulative distribution plots illustrating the portion of predictions within a given absolute error. Scatter plots show t-SNE projections of the latent embeddings of crystals. The embeddings are taken from the final attention pooling layer of structure-agnostic (c) and structure-based (d) versions of our model. The scatters are color-coded according to the predicted E_f. Identical perplexity (30) and same random initialisations are used when creating the t-SNE plots. (e) Scatter plot shows the correlation between the first principal components of structure-agnostic and structure-based material embeddings, and (f) depicts the same trend between the second principle components. Each scatter in plots (c)-(e) represents a material from the E_f test set.

materials in proximity are likely to be compositionally and structurally alike. This is quite compelling because it allows domain transferability at a reasonable fidelity. For example, structure-agnostic embedding of an undiscovered compound may be placed on the structure-based latent map and the neighbouring materials may be analysed to understand the possible crystal structure and the properties of the said hypothetical compound. This transferability was not possible between previous crystal graph and stoichiometry-only models due to contrasting ML model architectures and material descriptors. However, dedicated research is necessary to quantify the accuracy and validity of the specified strategy. Likewise, one has to perform such experiments in the original high-dimensional space rather than in the t-SNE or PCA reduced space for a more concrete analysis.

We note that training batch size has a considerable impact on the MAEs of all structure-based models. A batch size of 24 yields optimal results for both `Finder` and `CGCNN` in predicting formation energy, whereas `MegNet` requires a relatively large batch size of 128 to stabilize training. Small batch sizes introduce noise in the error gradient estimation because model weights are updated more frequently. This might be desirable in some cases to circumvent local minima in the error surface. A batch size of 128 moderately increases formation energy MAEs of `Finder` and `CGCNN` to 0.0365 and 0.0455, respectively. Refractive index prediction uses an optimal batch size of 24 for all models and a default batch size of 128 operates well on all other properties.

It is worth mentioning that MAEs reported in this work for the structure-based models on the MP database are slightly higher than those reported in original works.[11,12] This is likely because we eliminate structural polymorphs from our databases. This intercepts the distinct advantage of seeing the same composition with slightly different properties triggered by the polymorphs, eventually increasing the prediction error by a small degree. Different sizes and random generation of training and test databases may also be a contributing factor. We further evaluate our model on *MP-crystals-2018.6.1* E_f dataset used in the work of `MegNet` with same data division criterion[12] and observe a MAE of 0.0281 eV/atom for the test set, consistent with the original results, although the architecture of our model is not tuned on datasets containing polymorphs.

2.4 Ablation experiments

We perform ablation experiments to understand the causality of different components of our model and optimise its architecture. Such experiments are conducted mainly on structure-agnostic `Finder`, however, we further evaluate the structure-based model at critical points to ensure both variants are adequately optimised. Table 3 shows the results of ablation study on the E_f database. While the number of message passing layers does not have a noticeable impact on the performance of structure-agnostic model, structure-based model observes a significant performance gain with multiple message passing layers

compared to a solitary layer. Further increase of the number of message passing layers comes at the cost of degraded accuracy on small databases. As such, four message passing layers in composition-only domain increases the error in bulk modulus prediction by 5.3% relative to the default architecture (see Supporting Table S1).

Element embeddings of our model are transferred from ref.[54] Alternatively, we investigate one-hot element embeddings and observe a substantial dip in accuracy, particularly when the crystal structure is considered. This indicates node attributes that capture prior knowledge still help in navigating to a lower minimum in the error surface although this accuracy gap is expected to narrow down as the database size grows. Post-processing neural network is an essential component of our model as an exclusive message passing architecture inflates the error by up to 23%. We further note that including one standard convolutional layer in the post-processing network yields optimal results while adding more such layers impairs the performance. The number of rear dense layers and their widths are calibrated heuristically.

We then remove all attention blocks from our architecture and observe that the error rises by up to 11%. Likewise, capturing individual atom contributions is instrumental as some material properties depend more on the presence of certain elements compared to the others. In order to assess the contribution of our transformer-based self-attention variant to the model performance, we keep the `Roost`-like soft attention block in the global pooling layer and remove only the transformer self-attention section from the message passing layers. This results in a MAE of 0.0931 (8.5% surge) in the structure-agnostic arena, illustrating that the success of our model is mainly driven by the proposed architectural advancement.

	# Message passing layers			One-hot node embeddings	Post processing network removed	Attention components removed
	1	2	3			
Structure-agnostic Finder	0.0861	**0.0858**	0.0867	0.0876	0.1056	0.0882
Structure-based Finder	0.0393	**0.0342**	0.0342	0.0398	0.0403	0.038

Table 3: MAEs of different models considered in ablation study. At each experiment, all parameters are set to the default values as found in Supporting Table S1 except for the one being tested.

2.5 Epsilon-near-zero materials discovery as an application of Finder

Undoubtedly, the intimacy between chemical structures and graph neural networks produces excellent results in predicting various material properties. However, the potential of GNNs in predicting material properties in the form of a complex function is yet to be established. This renders a multi-output regression problem. Recently, GNNs have been successfully applied to predict the absorption spectra of three-cation metal oxides.[55] In a similar vein, a multi-class classification GNN is implemented to predict protein functions.[56] As a challenging application, we employ structure-agnostic `Finder` to predict frequency-dependent dielectric function of inorganic compounds and eventually locate epsilon-near-zero

(ENZ) candidates. ENZ materials possess a vanishingly small permittivity at a certain frequency that induces exceptional properties, some of which are still being experimented following theoretical predictions.[57] While structural ENZ materials such as metamaterials have been extensively studied, they achieve ENZ behaviour only as an effective property occurring on wavelengths larger than the size of structural unit, not to mention the increased fabrication cost and complexity. Hence, there is a growing interest in natural materials that exhibit ENZ phenomena, especially with low dielectric loss.

We extract a database of real (ε_{re}) and imaginary (ε_{im}) dielectric functions from the JARVIS repository. These are calculated using the OptB88vdW (OPT) DFT functional and shown to agree well with experimental data.[58] Duplicate compositions have been removed from this database by selecting the most stable polymorph, resulting in a total of 12,353 materials. While the dielectric constant can be anisotropic, the quantities for different directions such as *xx, yy, zz,* usually follow a similar trend and show equivalent resonance frequencies. Therefore, we only focus on the *xx* direction. ε_{re} and ε_{im} databases are divided into 80% training, 10% validation and 10% test sets, separately. We investigate the dielectric function prediction performance of `Finder` and `ResCNN` on the test set. Both models achieve respectable performance metrics with `Finder` outperforming `ResCNN` as expected (see Table 4).

Figure 6a and Figure 6b depict representative predictions for two selected materials from the test set. Note that `Finder` successfully captures several dielectric resonances of compositionally diverse materials (e.g. $Ba_2LiCu(CO_5)_2$ as shown in Figure 6b). What is more intriguing is that the predictions are based on a relatively small training database (9882 samples), and no structural information is incorporated in the process. Clearly, our model learns the complex mapping from composition to dielectric function, bypassing the need for crystal structure and the computational complexity of DFT which is further intensified by accurate functionals such as OPT.

The frequency range where $|\varepsilon_{re}| < 1$ is identified as the ENZ region. This is usually a narrow band positioned around the crossover energy point, the frequency at which the real part of permittivity crosses zero, ω_{co}. While all metals achieve the ENZ condition at the bulk plasma resonance typically in the UV band, present studies are focussed on investigating ENZ materials in the NIR range that is close to the telecommunications wavelengths (1550 nm), as well as visible range that is directly accessible by optical experiments. Although the ENZ condition is only reliant on the real permittivity, large imaginary permittivity values, that is high loss, severely suppress the ENZ effect. In this work, we predict ε_{re} and ε_{im} functions of materials in the MP database and report low loss ENZ candidates ($\varepsilon_{im} < 2$)[37] in NIR to UV band ($0.5 - 12.4$ eV) that are potentially stable ($E_{hull} < 25$ meV).

Figure 6c depicts the inferred ε_{im} vs ω_{co} dispersion. Evidently, the number of compositions with $\varepsilon_{im} < 2$ is extremely small compared to the composition space, making low loss ENZ materials discovery further challenging. We found 353 compositions from the MP database that satisfy above conditions. The

candidate list covers 80 periodic table elements. Interestingly, the predicted ENZ compositions include alkaline earth metal vanadates such as $Mg_2V_2O_7$ and $Ca_2V_2O_7$ that relate to recently identified low loss ENZ materials, namely, CaVO3 and SrVO3.[59] Strong electron-electron interactions present in such transition metal oxides can be capitalised to achieve ENZ condition in the visible spectrum. Unexpectedly, we found that 49 predicted ENZ materials contain vanadium and oxygen together, the most for any pair of periodic table elements. Other commonly appearing element pairs include Ca−O, Na−O and Fe−F (see Figure 6d). Linking these observations with already characterised ENZ correlated metals, we foresee vanadate compounds as an exciting class of materials for ENZ candidacy. Materials that feature a zero-permittivity wavelength in the NIR band are of great importance in telecommunications.[37] We identify two potentially stable new compositions, $CaV_2P_2O_9$ and $NaCr_2FeO_8$ that are predicted to exhibit low-loss ENZ properties in NIR region. Real and imaginary parts of the dielectric function as predicted by our model are shown in Figure 6e and 6f for the respective materials. E_{hull} and ε_{im} of both materials are well within the tolerable margins specified above. The full list of predicted ENZ compositions is provided as Supporting Data. We believe the search for functional ENZ materials has an expansive future especially considering the demonstrated potential of correlated metals.

	ε_{re}				ε_{im}			
	MAE	RMSE	R^2 score	MAD:MAE	MAE	RMSE	R^2 score	MAD:MAE
Finder	**0.69**	3.05	0.81	4.1	**0.72**	3.18	0.81	5.2
ResCNN	0.76	3.39	0.82	3.7	0.77	3.45	0.83	4.8

Table 4: Performance metrics of `Finder` and `ResCNN` on frequency-dependent dielectric function prediction. Both models are trained with the L_1 loss.

3 Discussion

Both structure-based and structure-agnostic branches of materials property prediction come with inherent pros and cons. Current ML models are limited to only one of the two branches owing to the little overlap between the material representations adopted in these two domains. It is our belief that this separation is merely due to contrasting design choices rather than a necessity. Unifying such approaches minimizes redundancies prompted by a plethora of material descriptors specific to each domain and enables constructing a single transferrable ML architecture.

In support of this objective, we propose formula graph, a systematic generalisation of composition-only and crystal structure dependent material representations. Our intuition is to denote individual atoms in a chemical formula as nodes in a graph. The only decisive fragment between composition-only and structure-based formula graphs is the edge attribute which is readily available as atomic spacings for the

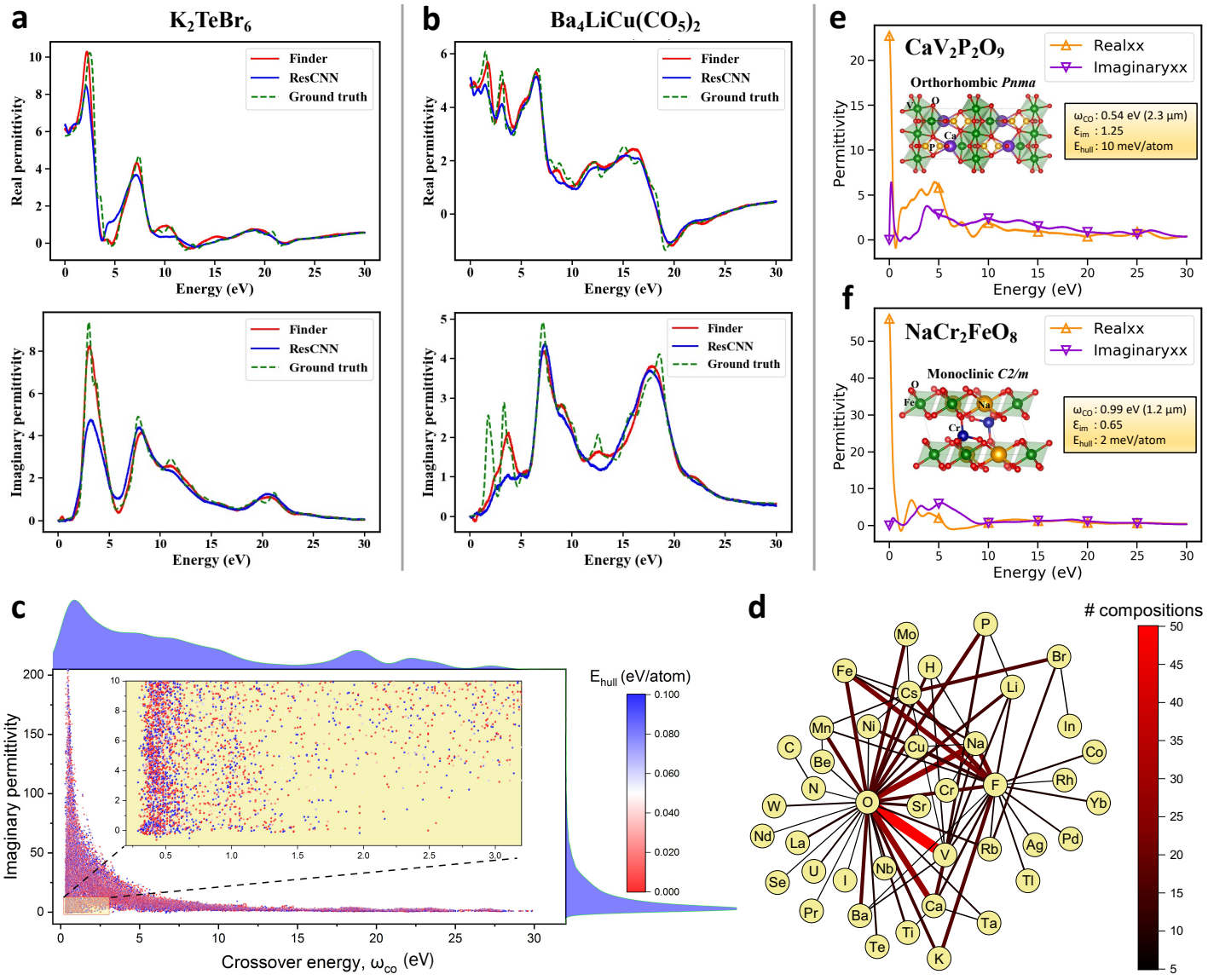

Figure 6: Epsilon-near-zero materials discovery from the MP database. Frequency-dependent ε_{re} and ε_{im} functions of two representative materials K_2TeBr_6 (a) and $Ba_4LiCu(CO_5)_2$ (b) as predicted by `Finder` and `ResCNN`. The x-axis represents the frequency in the units of photon energy. (c) Scatter plot shows the imaginary permittivity at the crossover energy point inferred from the predicted dielectric functions. (d) Network plot indicates element pairs that are present together in at least five predicted ENZ compositions. Each edge represents a pair of elements and the edge width is proportional to the number of element-pair appearances. (e) and (f) Show the predicted ε_{re} and ε_{im} of promising ENZ materials $CaV_2P_2O_9$ and $NaCr_2FeO_8$ along with their crystal structure.

latter and predicted during training for the former. We construct a self-attention driven message passing GNN and demonstrate that our model outperforms previous models irrespective of the representation domain in predicting various material properties.

Moreover, our model displays better sample efficiency and learning efficiency compared to other models. This makes it a frontrunner for small data learning tasks that are abundant in materials science. Additionally, our deep learning baseline model produces respectable results in many tasks. We reckon standard CNNs still have some scope left in materials informatics, especially owing to the use of simple descriptors and easier implementation.

Finally, we expose `Finder` to a challenging task of predicting the frequency-dependent dielectric function of inorganic compounds. Subsequently, we identify promising low loss ENZ materials that are of technological importance especially in optics and antenna engineering, demonstrating a real-world materials discovery application.

Our framework is not restricted to stoichiometric compounds. It can represent alloys, non-stoichiometric compounds or doped substances by converting the fractional element contributions to integer values. However, too small doping ratios multiply the size of formula graph and increase time and memory complexities, similar to how generating too large a supercell can make DFT calculations intractable. The same is true for alloys. As such, transforming a fractional formula of $A_{0.33}B_{0.67}$ to AB_2 as its integer form makes more sense than a naïve conversion to $A_{33}B_{67}$.

We view `Finder` as a potential distance matrix predictor that may help discover new crystal structures. This may be achieved, for example, by minimising the error between predicted edge attribute and the actual distance between corresponding atoms, instead of predicting a global material property. Alternatively, one might attempt to find a general mapping from EAM to distance matrix given $\mathcal{Z}$. However, the existence of such a function is not a known priori. Yet another potential avenue of improvement is transfer learning from structure-based `Finder` to a structure-agnostic task as opposed to same domain transfer learning common in materials informatics. Nonetheless, these are recognised as future research directions. We believe domain invariant frameworks such as `Finder` that incorporate methodological successes from other disciplines including NLP and computer vision inaugurate a truly interdisciplinary avenue of research in materials science.

4 Experimental Section

We tune the architecture and hyperparameters of `Finder` to an adequate level by heuristically selecting a pool of hyperparameters that allows sufficient degrees of freedom yet remain computationally tolerable. We eventually settle to an architecture composed of two message passing layers followed by a post processing residual neural network with one convolutional-1D layer and four dense layers having 512, 1024, 1024 and

256 units, respectively. The element embeddings are adopted from ref.[54] each having a dimension of 200. We realise that keeping the same dimension through our message passing layer improves the performance, although this is probed as a user-specified hyperparameter equivalent to the output shape of the preprocessing weight matrix W_{int}.

Function approximator networks ϕ_e and ϕ_m contain two hidden layers carrying 128 and 64 units. F_Q, F_K and F_V networks are all composed of individual weight matrices with a tunable output dimension defaulting to 200. Our global attention pooling component has pre- and post- processing layers each having 256-units. L_2 regularisation of 10^{-6} is applied to all weights. We employ tensor clipping to evade exploding gradient problem[60] which is one of the pitfalls of L_1 robust loss, despite its high empirical performance.

Rectified linear units (ReLU) is used as hidden layer activation function that is changed to linear activation for the output layer. We use Adam optimiser with an initial learning rate of 3x10^{-4} which is reduced by a factor of 0.999 at every iteration to allow finer convergence. Structure-agnostic models usually converge within 500 epochs with a batch size of 128 while structure-based models require about 1000 epochs to converge. Per-epoch timing for the E_f database is about 35 seconds for the former and 55 seconds for the latter on an RTX 2080 Ti graphics processing unit. `Finder` is implemented in *Keras*[61] on top of *Spektral* graph deep learning library.[62]

We use a cutoff distance of 4 Å as used in `MegNet`[12] to derive the crystal graph. Structure-based edge attribute is of length 20 stemmed by the Gaussian expansion of spatial distance that takes the basis $exp(-(r-r_0)^2/\sigma^2)$ centred at 20 equidistant points between 0 to 5 where $\sigma = 0.5$.[12] `Roost`, `MegNet` and `CGCNN` models are trained with recommended parameters from their respective repositories.[11,12,33] Additionally, we investigate a small batch size of 24 in addition to the default value of 128 for all structure-based models. The models are trained for 1200 epochs or until stopped by early stopping criteria. We note that because `MegNet` discards crystal graphs with isolated atoms, its training set size in this work is slightly smaller (67814) relative to the full training set size (68699). However, we stick to the default cut-off distance of 4 Å because increasing this value to 6 Å downgrades the performance as found in the original work[12] while multiplying the computational complexity by almost 3 times. According to the power law, such a marginal difference in training set sizes at that scale should have a negligible effect on the performance.

`RF_Magpie` model adopts the implementation from *scikit-learn*[63] with default parameters and the *Magpie* features are acquired from *Matminer* package.[64] `ResCNN` model is optimised to have four convolutional-1D layers containing 64, 128, 256 and 256 filters, respectively. A global max pooling layer is then placed to reduce the dimensionality and introduce local translation invariance. A set of postprocessing dense layers similar to that of `Finder` is appended with skip connections to complete our deep learning baseline architecture. The default parameters of `Finder` and `ResCNN` are given in Supporting Table S1 and Table S2, respectively.

Supporting Information

Supporting Information is available from the Wiley Online Library.

Acknowledgements

The authors acknowledge funding received by The Institution of Engineering and Technology (IET) under the AF Harvey Research Prize. This work is supported in part by EPSRC Software Defined Materials for Dynamic Control of Electromagnetic Waves (ANIMATE) grant (EP/R035393/1).

Author Contributions

A.I. designed the machine learning framework, performed data analysis and wrote the paper. Y.H. directed and coordinated the research. All authors discussed the results and reviewed the manuscript.

Competing Interests

The authors declare that they have no competing interests.

Data availability

The MP benchmark databases curated in this study are currently linked to our github repository and will be made available in Figshare upon acceptance. The list of predicted ENZ materials are included as Supporting Data. All other data needed to evaluate the findings of this study are present in the paper and/or the Supporting Information.

Code availability

The codes required to reproduce the results of this study will be made publicly available at https://github.com/ihalage/Finder.

References

[1] N. Hine, P. Haynes, A. Mostofi, C.-K. Skylaris, M. Payne, *Computer Physics Communications* **2009**, *180*, 7 1041.

[2] M. Bogojeski, L. Vogt-Maranto, M. E. Tuckerman, K.-R. Müller, K. Burke, *Nature Communications* **2020**, *11*, 1 5223.

[3] J. Schmidt, M. R. G. Marques, S. Botti, M. A. L. Marques, *npj Computational Materials* **2019**, *5*, 1 83.

[4] F. Ren, L. Ward, T. Williams, K. J. Laws, C. Wolverton, J. Hattrick-Simpers, A. Mehta, *Science Advances* **2018**, *4*, 4.

[5] B. Weng, Z. Song, R. Zhu, Q. Yan, Q. Sun, C. G. Grice, Y. Yan, W.-J. Yin, *Nature Communications* **2020**, *11*, 1 3513.

[6] P. Raccuglia, K. C. Elbert, P. D. F. Adler, C. Falk, M. B. Wenny, A. Mollo, M. Zeller, S. A. Friedler, J. Schrier, A. J. Norquist, *Nature* **2016**, *533*, 7601 73.

[7] Z. Chen, N. Andrejevic, T. Smidt, Z. Ding, Q. Xu, Y.-T. Chi, Q. T. Nguyen, A. Alatas, J. Kong, M. Li, *Advanced Science* **2021**, *8*, 12 2004214.

[8] V. L. Deringer, M. A. Caro, G. Csányi, *Advanced Materials* **2019**, *31*, 46 1902765.

[9] R. Nagai, R. Akashi, O. Sugino, *npj Computational Materials* **2020**, *6*, 1 43.

[10] L. Ward, A. Agrawal, A. Choudhary, C. Wolverton, *npj Computational Materials* **2016**, *2*, 1 16028.

[11] T. Xie, J. C. Grossman, *Phys. Rev. Lett.* **2018**, *120* 145301.

[12] C. Chen, W. Ye, Y. Zuo, C. Zheng, S. P. Ong, *Chemistry of Materials* **2019**, *31*, 9 3564.

[13] A. Ihalage, Y. Hao, *npj Computational Materials* **2021**, *7*, 1 75.

[14] R. Yuan, Y. Tian, D. Xue, D. Xue, Y. Zhou, X. Ding, J. Sun, T. Lookman, *Advanced Science* **2019**, *6*, 21 1901395.

[15] P. V. Balachandran, B. Kowalski, A. Sehirlioglu, T. Lookman, *Nature Communications* **2018**, *9*, 1 1668.

[16] T. Lookman, P. V. Balachandran, D. Xue, R. Yuan, *npj Computational Materials* **2019**, *5*, 1 21.

[17] F. Oviedo, Z. Ren, S. Sun, C. Settens, Z. Liu, N. T. P. Hartono, S. Ramasamy, B. L. DeCost, S. I. P. Tian, G. Romano, A. Gilad Kusne, T. Buonassisi, *npj Computational Materials* **2019**, *5*, 1 60.

[18] K. Ghosh, A. Stuke, M. Todorović, P. B. Jørgensen, M. N. Schmidt, A. Vehtari, P. Rinke, *Advanced Science* **2019**, *6*, 9 1801367.

[19] F. Dinic, K. Singh, T. Dong, M. Rezazadeh, Z. Wang, A. Khosrozadeh, T. Yuan, O. Voznyy, *Advanced Functional Materials n/a*, n/a 2104195.

[20] L. A. Griffin, I. Gaponenko, N. Bassiri-Gharb, *Advanced Materials* **2020**, *32*, 38 2002425.

[21] A. Ziletti, D. Kumar, M. Scheffler, L. M. Ghiringhelli, *Nature Communications* **2018**, *9*, 1 2775.

[22] N. Liu, A. Ihalage, H. Zhang, H. Giddens, H. Yan, Y. Hao, *J. Mater. Chem. C* **2020**, *8* 10352.

[23] R. Batra, L. Song, R. Ramprasad, *Nature Reviews Materials* **2021**, *6*, 8 655.

[24] J. Gilmer, S. S. Schoenholz, P. F. Riley, O. Vinyals, G. E. Dahl, In *Proceedings of the 34th International Conference on Machine Learning - Volume 70*, ICML'17. JMLR.org, **2017** 1263–1272.

[25] K. T. Schütt, H. E. Sauceda, P.-J. Kindermans, A. Tkatchenko, K.-R. Müller, *The Journal of Chemical Physics* **2018**, *148*, 24 241722.

[26] V. Fung, J. Zhang, E. Juarez, B. G. Sumpter, *npj Computational Materials* **2021**, *7*, 1 84.

[27] S.-Y. Louis, Y. Zhao, A. Nasiri, X. Wang, Y. Song, F. Liu, J. Hu, *Phys. Chem. Chem. Phys.* **2020**, *22* 18141.

[28] J. Klicpera, J. Groß, S. Günnemann, *CoRR* **2020**, *abs/2003.03123*.

[29] K. Choudhary, B. DeCost, *npj Computational Materials* **2021**, *7*, 1 185.

[30] Z. Qiao, M. Welborn, A. Anandkumar, F. R. Manby, T. F. Miller, *The Journal of Chemical Physics* **2020**, *153*, 12 124111.

[31] A. P. Bartók, R. Kondor, G. Csányi, *Phys. Rev. B* **2013**, *87* 184115.

[32] N. Artrith, A. Urban, G. Ceder, *Phys. Rev. B* **2017**, *96* 014112.

[33] R. E. A. Goodall, A. A. Lee, *Nature Communications* **2020**, *11*, 1 6280.

[34] A. Vaswani, N. Shazeer, N. Parmar, J. Uszkoreit, L. Jones, A. N. Gomez, L. u. Kaiser, I. Polosukhin **2017**, *30*.

[35] K. Choudhary, K. F. Garrity, A. C. E. Reid, B. DeCost, A. J. Biacchi, A. R. Hight Walker, Z. Trautt, J. Hattrick-Simpers, A. G. Kusne, A. Centrone, A. Davydov, J. Jiang, R. Pachter, G. Cheon, E. Reed, A. Agrawal, X. Qian, V. Sharma, H. Zhuang, S. V. Kalinin, B. G. Sumpter, G. Pilania, P. Acar, S. Mandal, K. Haule, D. Vanderbilt, K. Rabe, F. Tavazza, *npj Computational Materials* **2020**, *6*, 1 173.

[36] O. Reshef, I. De Leon, M. Z. Alam, R. W. Boyd, *Nature Reviews Materials* **2019**, *4*, 8 535.

[37] N. Kinsey, C. DeVault, A. Boltasseva, V. M. Shalaev, *Nature Reviews Materials* **2019**, *4*, 12 742.

[38] J. Park, J.-H. Kang, X. Liu, M. L. Brongersma, *Scientific Reports* **2015**, *5*, 1 15754.

[39] A. Korobenko, S. Saha, A. T. K. Godfrey, M. Gertsvolf, A. Y. Naumov, D. M. Villeneuve, A. Boltasseva, V. M. Shalaev, P. B. Corkum, *Nature Communications* **2021**, *12*, 1 4981.

[40] S. Haim, O. Kevin, W. Z. Jing, S. Alessandro, Y. Xiaobo, Z. Xiang, *Science* **2013**, *342*, 6163 1223.

[41] N. Kinsey, C. DeVault, J. Kim, M. Ferrera, V. M. Shalaev, A. Boltasseva, *Optica* **2015**, *2*, 7 616.

[42] G. Kafaie Shirmanesh, R. Sokhoyan, R. A. Pala, H. A. Atwater, *Nano Letters* **2018**, *18*, 5 2957.

[43] A. A. Emery, C. Wolverton, *Scientific Data* **2017**, *4*, 1 170153.

[44] G. Hautier, S. P. Ong, A. Jain, C. J. Moore, G. Ceder, *Phys. Rev. B* **2012**, *85* 155208.

[45] J. Hestness, S. Narang, N. Ardalani, G. F. Diamos, H. Jun, H. Kianinejad, M. M. A. Patwary, Y. Yang, Y. Zhou, *CoRR* **2017**, *abs/1712.00409*.

[46] G. Lambard, E. Gracheva, *Machine Learning: Science and Technology* **2020**, *1*, 2 025004.

[47] J. M. Crowley, J. Tahir-Kheli, W. A. Goddard, *The Journal of Physical Chemistry Letters* **2016**, *7*, 7 1198.

[48] I. Petousis, W. Chen, G. Hautier, T. Graf, T. D. Schladt, K. A. Persson, F. B. Prinz, *Phys. Rev. B* **2016**, *93* 115151.

[49] M. de Jong, W. Chen, T. Angsten, A. Jain, R. Notestine, A. Gamst, M. Sluiter, C. Krishna Ande, S. van der Zwaag, J. J. Plata, C. Toher, S. Curtarolo, G. Ceder, K. A. Persson, M. Asta, *Scientific Data* **2015**, *2*, 1 150009.

[50] J. P. Perdew, K. Burke, M. Ernzerhof, *Phys. Rev. Lett.* **1996**, *77* 3865.

[51] G. E. Scuseria, *Proceedings of the National Academy of Sciences* **2021**, *118*, 35.

[52] Á. Morales-García, R. Valero, F. Illas, *The Journal of Physical Chemistry C* **2017**, *121*, 34 18862.

[53] L. van der Maaten, G. Hinton, *Journal of Machine Learning Research* **2008**, *9*, 86 2579.

[54] V. Tshitoyan, J. Dagdelen, L. Weston, A. Dunn, Z. Rong, O. Kononova, K. A. Persson, G. Ceder, A. Jain, *Nature* **2019**, *571*, 7763 95.

[55] S. Kong, D. Guevarra, C. P. Gomes, J. M. Gregoire, *Applied Physics Reviews* **2021**, *8*, 2 021409.

[56] V. Gligorijević, P. D. Renfrew, T. Kosciolek, J. K. Leman, D. Berenberg, T. Vatanen, C. Chandler, B. C. Taylor, I. M. Fisk, H. Vlamakis, R. J. Xavier, R. Knight, K. Cho, R. Bonneau, *Nature Communications* **2021**, *12*, 1 3168.

[57] A. Marini, F. J. García de Abajo, *Scientific Reports* **2016**, *6*, 1 20088.

[58] K. Choudhary, Q. Zhang, A. C. Reid, S. Chowdhury, N. Van Nguyen, Z. Trautt, M. W. Newrock, F. Y. Congo, F. Tavazza, *Scientific Data* **2018**, *5*, 1 180082.

[59] L. Zhang, Y. Zhou, L. Guo, W. Zhao, A. Barnes, H.-T. Zhang, C. Eaton, Y. Zheng, M. Brahlek, H. F. Haneef, N. J. Podraza, M. H. W. Chan, V. Gopalan, K. M. Rabe, R. Engel-Herbert, *Nature Materials* **2016**, *15*, 2 204.

[60] R. Pascanu, T. Mikolov, Y. Bengio, In S. Dasgupta, D. McAllester, editors, *Proceedings of the 30th International Conference on Machine Learning*, volume 28 of *Proceedings of Machine Learning Research*. PMLR, Atlanta, Georgia, USA, **2013** 1310–1318, URL https://proceedings.mlr.press/v28/pascanu13.html.

[61] F. Chollet, et al., Keras, **2015**, URL https://keras.io.

[62] D. Grattarola, C. Alippi, *Comp. Intell. Mag.* **2021**, *16*, 1 99–106.

[63] F. Pedregosa, G. Varoquaux, A. Gramfort, V. Michel, B. Thirion, O. Grisel, M. Blondel, P. Prettenhofer, R. Weiss, V. Dubourg, et al., *Journal of machine learning research* **2011**, *12*, Oct 2825.

[64] L. Ward, A. Dunn, A. Faghaninia, N. E. Zimmermann, S. Bajaj, Q. Wang, J. Montoya, J. Chen, K. Bystrom, M. Dylla, K. Chard, M. Asta, K. A. Persson, G. J. Snyder, I. Foster, A. Jain, *Computational Materials Science* **2018**, *152* 60.